Available online at www.sciencedirect.com
SCIENCE DIRECT®
International Journal of Rock Mechanics & Mining Sciences 42 (2005) 388–401
International Journal of Rock Mechanics and Mining Sciences
www.elsevier.com/locate/ijrmms

Characterizing the deformation behavior of Tertiary sandstones

M.C. Weng, F.S. Jeng*, T.H. Huang, M.L. Lin

Department of Civil Engineering, National Taiwan University, Taipei, 1, Sec. 4, Roosevelt Road, Taipei 10617, Taiwan

Accepted 22 December 2004

Abstract

Tertiary sandstones possess deformational behavior different from hard rocks, especially the relatively larger amount of volumetric dilation during shearing. Such excess dilation contributes to the increase of crown settlement during tunnel excavation and accounts for several cases of tunnel squeezing within Tertiary sandstones. Therefore, the deformation behavior of Tertiary sandstones sampled from more than 13 formations was studied. To distinguish the volumetric deformation induced by hydrostatic stress or by shear stress as well as to decompose the elastic and the plastic components of strains, special experimental techniques, including pure shear tests and cycles of loading–unloading were applied.

The experimental results reveal that the deformation of Tertiary sandstone exhibits the following characteristics: (1) significant amount of shear dilation, especially elastic shear dilation; (2) non-linear elastic and plastic deformation; (3) plastic deformation occurs prior to the failure state. Furthermore, features of plastic deformation were inferred from experimental results and, as a result, the geometry of plastic potential surface and the hardening rule were accordingly determined. A constitutive model, involving nonlinear elastic/plastic deformation and volumetric deformation induced by shear stress, is proposed. This proposed model simulates the deformational behavior for the shear-dilation-typed rocks reasonably well. Furthermore, tests on the versatility of the proposed model, including varying hydrostatic stress and stress paths, indicate that the proposed model is capable of predicting deformational behavior for various conditions.

Keywords: Sandstone; Constitutive model; Deformation; Shear dilation

1. Introduction

Tertiary sandstones have a digenetic age of no more than 70 million years and such relatively short rock forming period is insufficient to classify them as hard rocks. For instance, the typical strength of Tertiary sandstones in Taiwan ranges from 10 to 80 MPa [1].

While tunneling through the Tertiary strata, several unsuccessful cases were reported [2]. Difficulties, including severe squeezing and raveling, were encountered during construction of these tunnels. For instance, a crown settlement of 180 cm of a 12.4 m wide highway tunnel passing through a faulted zone of Tertiary formations was reported. A crown settlement ranging from 14 to 30 cm occurred in several sections of the tunnels under construction, in which Tertiary sandstone (Mushan Formation) was encountered. The crown settlement in other sandstones' strata is often within several centimeters. Therefore, the deformational characteristics of Tertiary sandstones should be involved while the deformation of a constructing tunnel is analyzed.

When compared to hard rock, it was found that the deformational behavior of Tertiary sandstones is characterized by large amount of nonlinear deformation, shear dilation and plastic deformation prior to the failure state [3–5]. Jeng et al. [6] compared the mechanical properties of sandstone, the uniaxial compressive strength (UCS) and the reduction of strength due to wetting ($R = \mathrm{UCS_{dry}}/\mathrm{UCS_{wet}}$) with the petrographic features of the 13 sandstones listed in Table 1,

*Corresponding author. Tel./fax: +886 2 2364 5734.
E-mail address: fsjeng@ntu.edu.tw (F.S. Jeng).

1365-1609/$ - see front matter © 2005 Elsevier Ltd. All rights reserved.
doi:10.1016/j.ijrmms.2004.12.004

Nomenclature

α_1	hardening rule parameter for Cap model
α_f	slope of F_1
α_d	state variable of proposed model
b_1	elastic constant of proposed model
b_2	elastic constant of proposed model
b_3	elastic constant of proposed model
β_1	hardening rule parameter for proposed model
β_2	hardening rule parameter for proposed model
β_3	hardening rule parameter for proposed model
β_4	hardening rule parameter for proposed model
CTC	conventional triaxial compression test
ε_{ij}	second strain tensor
$\varepsilon^e_{v,p}$	elastic volume strain induced by hydrostatic stress
$\varepsilon^e_{v,s}$	elastic volume strain induced by shear stress
e_{ij}	second deviatoric strain tensor
ε_v	volume strain
$d\varepsilon^p$	increment of plastic strain, $d\varepsilon^p = \sqrt{d\varepsilon^p_{ij}\, d\varepsilon^p_{ij}}$
$F(I_1, J_2)$	yield surface
$G(I_1, J_2)$	plastic potential surface
G	shear modulus
G_0	initial shear modulus
γ	shear strain, $\gamma = 2\sqrt{J_2'} = \sqrt{2 \cdot e_{ij} e_{ji}}$
γ^e	elastic shear strain
γ^p	plastic shear strain
γ^t	total shear strain
γ_d	square of slope of failure envelope F
η_1	hardening rule parameter for cap model
J_2	second deviatoric stress invariant, $J_2 = \frac{1}{2} s_{ij} s_{ji}$
J_2'	second deviatoric strain invariant, $J_2' = \frac{1}{2} e_{ij} e_{ji}$
K	bulk modulus
k_f	interception of F_1
λ	positive scalar factor of proportionality
m	parameter for plastic potential surface
Ω	strain energy density function
p	hydrostatic stress $p = \frac{1}{3} I_1 = \frac{1}{3} \sigma_{kk}$ (MPa)
PS	pure shear test
R	strength reduction ratio $= UCS_{wet}/UCS_{dry}$
RTE	reduced triaxial extension test
R_c	axis ratio defined by Cap model
s_{ij}	second deviatoric stress tensor
σ_{ij}	second stress tensor
T	interception of failure envelope with I_1 axis
UCS	uniaxial compressive strength (MPa)

Superscripts

e	elastic deformation
p	plastic deformation
t	total deformation

Table 1
Sandstones of this research

Formation	Classification (Pettijohn et al., 1987)	Geological age	Sedimentary facies	Remark
WGS1	Lithic graywacke	Oligocene	Marine–terrestrial mixed facies	
WGS2	Lithic graywacke	Oligocene	Marine–terrestrial mixed facies	Apparent preferred orientation
MS1	Lithic graywacke	Miocene	Littoral facies	
MS2	Lithic graywacke	Miocene	Littoral facies	
MS3	Lithic graywacke	Miocene	Littoral facies	Apparent preferred orientation
TL1	Lithic graywacke	Miocene	Marine facies	
TL2	Lithic graywacke	Miocene	Marine facies	
ST	Lithic graywacke	Miocene	Littoral facies	
NK	Lithic graywacke	Miocene	Marine facies	
TK	Lithic graywacke	Miocene	Littoral facies	Apparent preferred orientation
SFG1	Quartzwacke	Miocene	Littoral facies	
SFG2	Lithic graywacke	Miocene	Littoral facies	Apparent preferred orientation, rich mica content
CL	Lithic graywacke	Pliocene	Littoral facies	Rich calcite content

and found that these Tertiary sandstones can be classified in terms of Grain area ratio (GAR) and porosity (n), as illustrated in Fig. 1. Two groups of sandstones, termed as *Type A* and *Type B* (with $R > 0.5$ and $R \leqslant 0.5$, respectively), have been identified. Comparing to *Type A*, *Type B* sandstone is characterized by greater degree of deformation (or being "softer") and by having a more significant reduction not only in strength but also in stiffness, as shown in Fig. 2. This characteristic highlights that *Type B* can be the problematic rock type, which is prone to tunnel squeezing.

This paper explores the deformational behavior of Tertiary sandstones in details. In addition to the above-mentioned research results, the work focuses on the following aspects:

1. To characterize the deformational behavior of Tertiary sandstones, including elastic and plastic

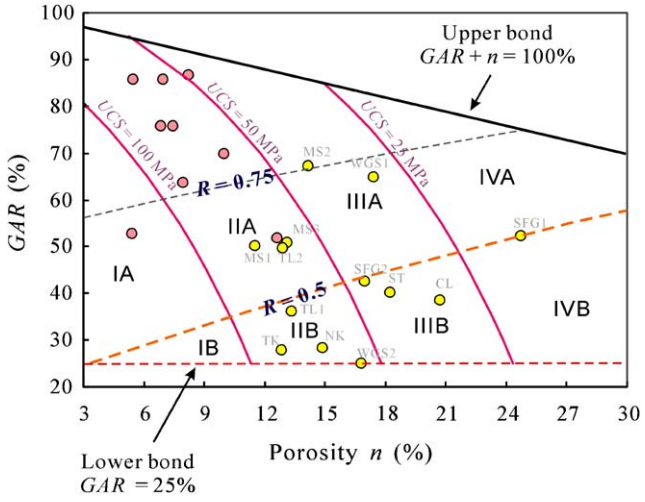

Fig. 1. Geotechnical classification of the studied sandstones in terms of n and GAR. The empirical UCS and R are shown by solid and dashed contour lines. The formation name of each sandstone is marked near each symbol. The sandstone is classified on one hand in terms of n and GAR, which affects its strength (UCS) and in terms of degree of wetting softening (R) on the other hand. Accordingly, the sandstones are classified into two groups: *Type A* ($R>0.5$) and *Type B* ($R\leqslant 0.5$). The classification of strength (*Types I–IV*) is based on the definition of ISRM (1981).

components of deformation for both volumetric and shear deformation;

2. To distinguish the volumetric deformation induced by hydrostatic stress or shear stress so that the contribution of shear dilation can be clarified.
3. To propose a constitutive model able to describe the deformational characteristics of Tertiary sandstones, for example, the elastic shear dilation.
4. To validate the proposed model, the predictions for various testing conditions, including stress paths and different hydrostatic pressures, are compared to actual test results.

Furthermore, to further differentiate the proposed constitutive model from other geo-material models, the simulations of other models, including the Drucker–Prager (DP) model and the cap model are compared with the proposed model, which also reveals the distinct deformational features of the Tertiary sandstones.

2. Set-up of experimental study

The deformation of sandstone, soft rocks or cemented soil has been explored by means of conventional triaxial compression tests (CTC), simple shear tests (SS) and triaxial extension tests (TE) under hydrostatic pressure from several kPa's to 27.6 MPa [7–10]. Based on the studied behavior, theoretical constitutive models

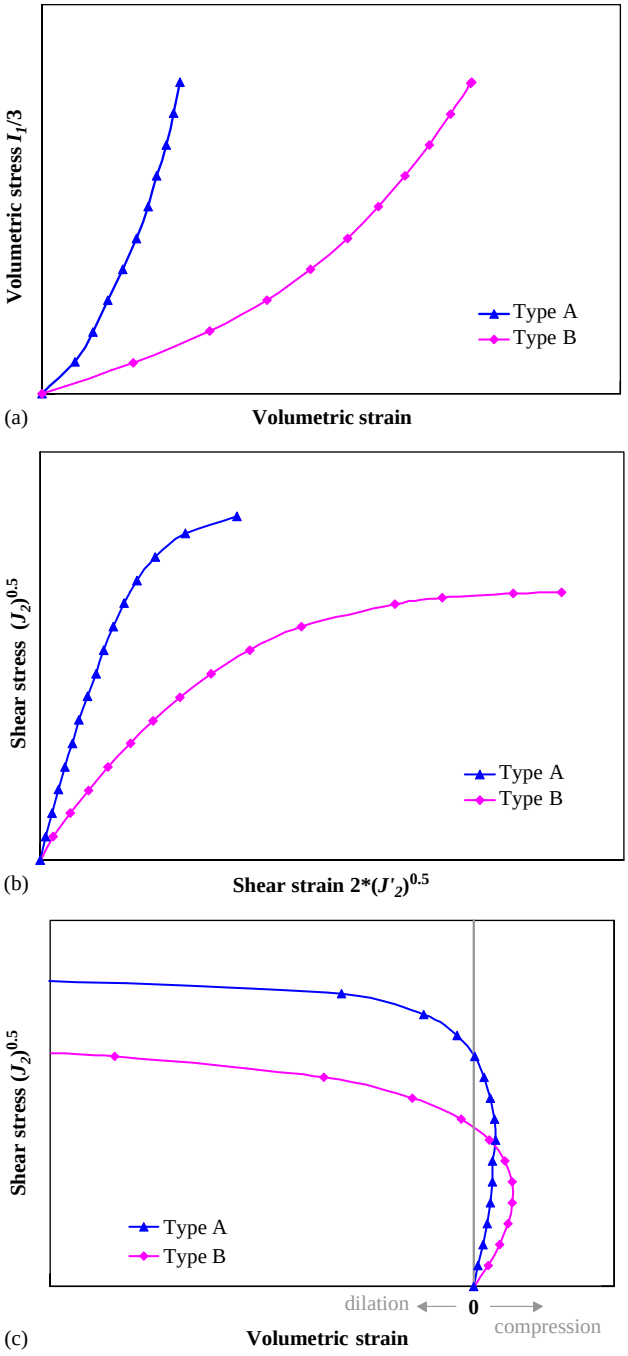

Fig. 2. Typical deformational behavior of the two types of Tertiary sandstones. Compared to *Type A* sandstone (MS2), *Type B* sandstone (WGS2) is characterized by more volumetric and shear deformation and less shear strength as well. $J'_2(=\frac{1}{2}e_{ij}e_{ij}; e_{ij}$ =second deviatoric strain tensor) is a measure of shear strain. (a) Volumetric strain induced by volumetric stress, (b) shear strain induced by shear stress and (c) volumetric strain induced by shear stress.

were accordingly proposed [7–9,11–13]. A review on previous works [14–20] has been provided by Desai and Salami [8].

Since shear dilation was of concern especially when dealing with tunnel squeezing and was reported as a

result of the opening of micro-cracks due to shearing [21–24], this research focused on identifying the volumetric deformation induced by shearing from hydrostatic stress. Stress-path-controlled tests, with the applications of hydrostatic stress and shear stress separated into two stages, were adopted so that the influence of hydrostatic stress and shearing on volumetric stress could be clearly distinguished.

Secondly, the components of elastic and plastic strains were decomposed to distinguish the contribution of each component to the total strain, which is essential when establishment of a constitutive model is intended. Cycles of loading unloading were performed to identify the elastic and the plastic components of strains at various stages of loading.

The specimens were loaded in a triaxial cell, to which the axial pressure (σ_1) and the confining pressure (σ_3) were applied, under room temperature. The triaxial cell was able to sustain the hydrostatic pressure up to 175 MPa. A pressure transducer monitored the hydrostatic pressure with an accuracy of 0.1 MPa. The axial load was provided by a high stiffness MTS loading frame, which has a maximum load and stiffness of 4448 kN and 13.1×10^9 N/m, respectively. Both the axial stress and the hydrostatic stress were servo-controlled so that tests with various stress paths would be feasible. The load was applied at a rate of 5 MPa/min.

The physical and mechanical properties of the studied sandstones were measured according to the methods suggested by ISRM [25]. The specimen size was 5.5 cm in diameter and 12.5 cm in height. The specimen was oven-dried (105 °C) to remove its natural water content. The longitudinal and transverse types of deformation were separately measured by a full Wheatstone bridge consisted of four strain gages, which were capable of measuring strains up to 2% with an accuracy of ± 0.85 (μm/m)/°C.

In Fig. 3 p $\left(=\frac{1}{3}I_1=\frac{1}{3}\sigma_{kk}\right)$ and $\sqrt{J_2}$ ($J_2=\frac{1}{2}S_{ij}S_{ij}$; S_{ij} = second deviatoric stress tensor) are measures of hydrostatic stress and shear stress, respectively. The specimen was first applied with hydrostatic stress (volumetric stress) along a stress path OA, followed by subsequent shearing. If the hydrostatic stress is not altered during the subsequent shearing, a pure shear (PS; path AC) condition is achieved and the volumetric strain induced in this stage of loading is surely the shear dilation/contraction [26–30]. Furthermore, to verify the applicability of the proposed constitutive model, other stress paths, including CTC (path AB) and reduced triaxial extension tests (RTE; path AD and path AE), as shown in Fig. 3, were also conducted [31].

Moreover, petrographic analysis, X-ray diffraction tests (XRD) and SEM observation were also conducted in this research.

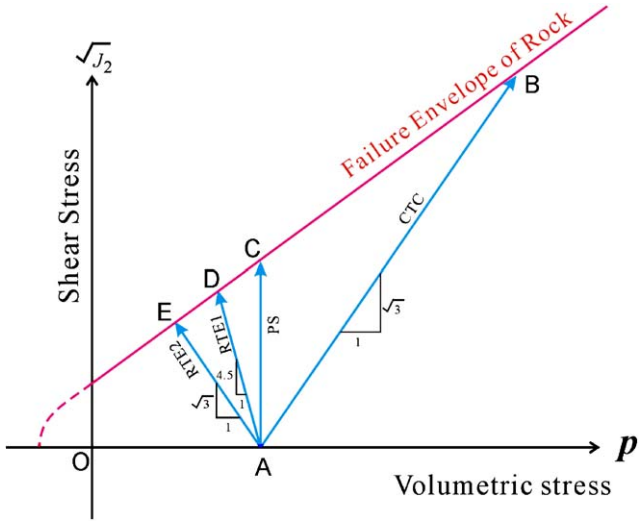

Fig. 3. Schematic illustration of the conducted stress paths. PS = pure shear test, CTC = conventional triaxial compression test, RTE = reduced triaxial extension tests.

3. Deformation characteristics of Tertiary sandstone

The physical properties of the tested sandstones are summarized in Table 2. In general, the studied sandstones are mainly composed of quartz (greater than 75%) with minor content of rock fragments and very little of feldspar (less than 5%); accordingly, these sandstones are classified as lithic graywacke or quartzwacke based on Pettijohn's definition [32]. The porosities range from 11% to 25%.

The mechanical properties of sandstones, including uniaxial strength and Young's modulus, are listed in Table 3. A fairly wide spectrum of mechanical behavior was obtained, in which the dry and wet uniaxial compressive strengths varied from 7–86 and 3–45 MPa, respectively. The (dry) strength was thus classified from low strength to medium strength, based on ISRM [25] definition. Remarkably, significant wetting softening could be observed, either in strength or in stiffness. The reduction ratio R ranged from 0.85 to as low as 0.14.

Fig. 4 illustrates the results of a PS test (path OAC in Fig. 3). During the hydrostatic loading (path OA), the bulk modulus increased as hydrostatic stress increased and it resulted in a nonlinear deformation curve, as shown in Fig. 4a. When cycles of loading, unloading and reloading were applied, the results showed that plastic volumetric strain existed. Based on the plastic strain revealed by the cycles of loading, the elastic deformation and the plastic deformation, at all stages along a controlled stress path, could be decomposed, as shown in Fig. 4.

In addition to the volumetric strain induced by the hydrostatic stress shown in Fig. 4a, Fig. 4b illustrates the shear strain (defined as $2\sqrt{J_2'}$ ($J_2'=\frac{1}{2}e_{ij}e_{ij}$; e_{ij} = second deviatoric strain tensor) induced by pure

Table 2
Physical properties of the studied sandstones

Formation	γ_d (g/cm^3)	G_s	n (%)	GAR (%)	Matrix (%)	Mineralogy of grains		
						Quartz (%)	Feldspar (%)	Rock fragment (%)
WGS1	2.19	2.66	17.4	65.0	17.6	90.3	0.0	9.7
WGS2	2.26	2.72	16.7	25.3	58.0	85.8	0.0	7.2
MS1	2.24	2.52	11.5	50.4	38.2	88.0	0.2	10.3
MS2	2.28	2.66	14.1	67.5	18.5	90.7	0.2	9.0
MS3	2.32	2.67	13.1	51.0	35.9	85.0	2.3	12.2
TL1	2.36	2.72	13.1	36.4	50.5	86.5	1.7	9.9
TL2	2.35	2.70	12.8	50.0	37.2	87.3	0.7	9.7
ST	2.18	2.67	18.2	40.4	41.4	77.7	4.4	12.7
NK	2.31	2.71	14.8	28.6	56.6	90.0	2.3	5.6
TK	2.30	2.65	12.8	28.2	59.0	84.5	0.5	13.0
SFG1	2.01	2.66	24.6	52.6	22.8	95.6	0.8	3.0
SFG2	2.21	2.66	16.9	42.8	40.4	78.4	1.6	8.9
CL	2.14	2.70	20.7	39.4	40.0	83.7	1.0	5.5

Table 3
Mechanical properties of sandstones

Formation	UCS_{dry} (MPa)	UCS_{wet} (MPa)	R	Strength classification ISRM (1981)	E_{dry} (GPa)	E_{wet} (GPa)	E_{wet}/E_{dry}	Shear dilation	No. specimen	
									Dry	Sat
WGS1	34.1	25.4	0.74	Moderate	11.9	4.4	0.37	Yes	8	9
WGS2	47.5	6.7	0.14	Moderate	5.0	1.6	0.32	Yes	10	8
MS1	48.5	28.9	0.60	Moderate	7.6	3.4	0.45	Yes	15	2
MS2	37.1	28.3	0.76	Moderate	12.7	10.0	0.79	Yes	27	23
MS3	82.7	43.3	0.52	Medium	14.0	9.9	0.71	Yes	3	3
TL1	68.7	23.2	0.34	Medium	9.7	4.3	0.44	Yes	11	9
TL2	77.5	44.2	0.57	Medium	12.2	7.3	0.60	Yes	3	3
ST	38.4	7.8	0.20	Moderate	5.6	1.6	0.29	Yes	5	3
NK	86.0	43.2	0.50	Medium	12.1	8.1	0.67	Yes	4	3
TK	69.0	29.4	0.43	Medium	5.2	2.2	0.43	Yes	10	2
SFG1	14.5	12.2	0.84	Low strength	2.6	2.2	0.85	Yes	3	3
SFG2	46.4	19.9	0.43	Moderate	5.2	2.5	0.48	Yes	3	3
CL	19.9	3.1	0.16	Low strength	—	—	—	Yes	7	6

Remarks: The strength reduction ratio R due to wetting softening is defined as: $R = UCS_{wet}/UCS_{dry}$.
Shear dilation occurs for all tests on both dry and wet specimens.

shearing (path AC). The elastic component is relatively linear when compared to the plastic component. When the stress path approached the failure envelope, namely the failure state, significant increases of plastic shear strain occurred, as shown in Fig. 4b, while the elastic component was linearly on the increase.

Fig. 4c shows the volumetric strain induced by shearing. The total strain experienced contraction and was followed by dilation above point A, as marked in Fig. 4c. After decomposing of elastic and plastic strains, it was found that elastic deformation tended to dilate throughout the shearing process while the plastic deformation went through contraction and then dilation. Therefore, if the establishment of a representative constitutive model for such sandstone is intended, shear dilation should be considered in addition to the conventional elasticity, to which pure shearing would induce no volumetric deformation.

As long as the plastic strain, including volumetric strain shown in Fig. 4a and c and shear strain shown in Fig. 4b, is obtained, the increments of plastic strains along any particular stress path (CTC or PS) can be presented as vectors shown in Fig. 5. Fig. 5 reveals the following characteristics of plastic deformation of sandstone:

(a) Plastic deformation exists prior to the failure state. Concerning this, a plastic potential surface (or a cap) in addition to the failure envelope is necessary for describing the deformation behavior of sandstone [6].
(b) When approaching failure state, these plastic deformation vectors tend to be perpendicular to the

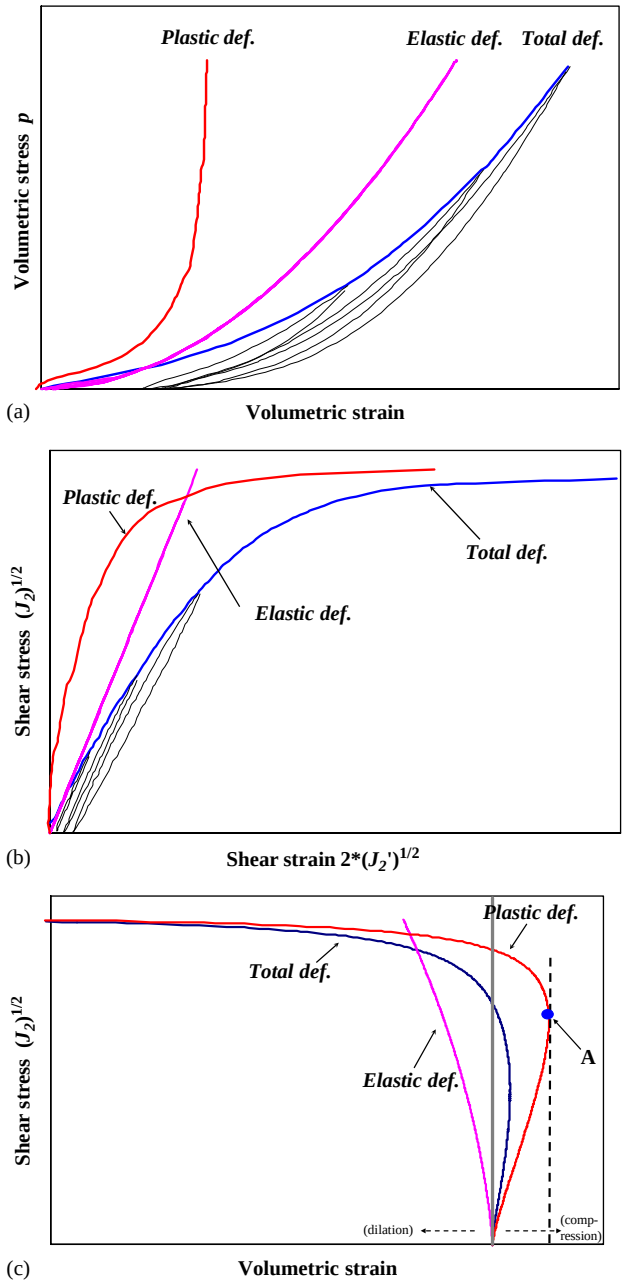

Fig. 4. Schematic illustration of typical deformation curves. Cycles of loading–unloading–reloading, which are indicated by gray lines, were applied to identify plastic deformation in separate stages of loading so that the total strain could be decomposed into elastic and plastic components, as shown in the figure. (a) Volumetric strain induced by hydrostatic stress (Path OA in Fig. 3) (b) Shear strain induced by shear stress (Paths AC in Fig. 3) (c) Volumetric strain induced by shear stress (Path AC in Fig. 3).

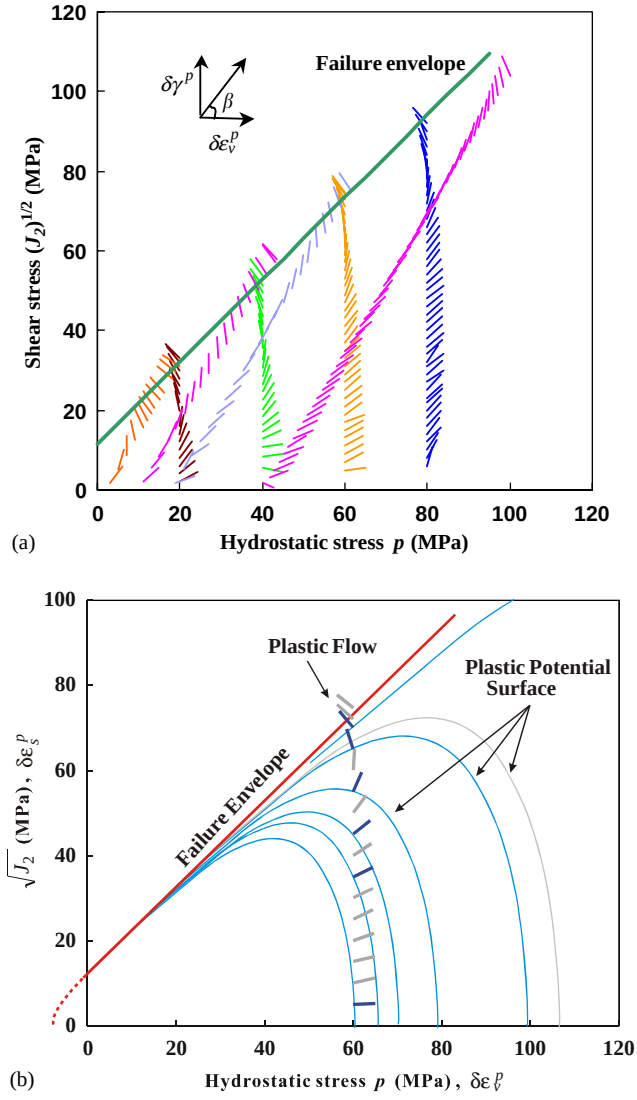

Fig. 5. Vectors of plastic strain increments during triaxial testing. (a) Vectors obtained from various stress paths. (b) Vector obtained from the pure shear test. The final vector (when the stress path meet the failure envelope) tends to be perpendicular to the failure envelope, which indicates a typical associated rule of plastic flow. A conceptual plastic potential surface is also plotted, provided the associated flow rule is assumed. This conceptual plastic potential surface would propagate upon subsequent increases of loading. It should be noticed that all the plastic potential surfaces have a similar geometry; i.e. not evolving of such surface is necessary.

failure envelope of sandstone, regardless the stress paths. That is, the plastic deformation at failure state appears to meet with the so-called associated flow rule. Therefore, a plastic potential surface with geometry illustrated by Fig. 5b, in which plastic deformation vectors meet with the associated flow rule, can be assumed. This plastic potential surface would propagate upon increases of loading and during the loading process. The vector continues to be perpendicular to this plastic potential surface and eventually be perpendicular to the failure envelope. Therefore, the plastic potential surface should have a tangent contact with the failure envelope, as shown in Fig. 5b.

(c) Inferred from the comparison of the experimental results shown in Fig. 5a with the plastic potential surfaces shown in Fig. 5b, it can be asserted that the

plastic potential surfaces tend to have a similar geometry, except that differ in sizes.

4. Proposed constitutive model

Given the deformational behavior of sandstone observed during the experimental study, a constitutive model can accordingly be developed to describe the aforementioned behavior found in this study. As the sandstone possesses both elastic and plastic deformation, the total strain tensor can thus be expressed in terms of these two components as

$$\varepsilon_{ij}^{t} = \varepsilon_{ij}^{e} + \varepsilon_{ij}^{p}, \tag{1}$$

where ε_{ij}^{t}, ε_{ij}^{e} and ε_{ij}^{p} are total strain tensor, elastic strain tensor and plastic strain tensor, respectively.

4.1. Elastic component of deformation

In view of the non-linear elastic behavior shown in Fig. 4a and c, a Green elastic model (or hyper-elastic model) is adopted [31]. On the basis of such a model, the strain tensor can be determined using strain energy density function Ω partially differentiated by the stress tensor σ_{ij} as the following expression:

$$\varepsilon_{ij}^{e} = \frac{\partial \Omega}{\partial \sigma_{ij}}. \tag{2}$$

Fig. 4 illustrates that the studied sandstones exhibit non-linear, elastic volumetric deformation, induced either by hydrostatic stress (Fig 4a) or by shear stress (Fig. 4c) and linear shear deformation (induced by shear stress; Fig. 4b). Given such deformational behavior on one hand and the nature of Green model (Eq. (2)) on the other hand, a strain energy density function Ω is accordingly proposed as

$$\Omega = b_1 I_1^{3/2} + b_2 I_1 J_2 + b_3 J_2, \tag{3}$$

where b_1, b_2 and b_3 are material constants.

Substituting Eq. (3) into Eq. (2), the elastic strain tensor ε_{ij}^{e} has the following form:

$$\varepsilon_{ij}^{e} = \frac{\partial \Omega}{\partial \sigma_{ij}} = (\tfrac{3}{2} b_1 I_1^{1/2} + b_2 J_2)\delta_{ij} + (b_2 I_1 + b_3) s_{ij}. \tag{4}$$

According to Eq. (4), the volumetric strain can be obtained as

$$\varepsilon_{v}^{e} = \varepsilon_{11}^{e} + \varepsilon_{22}^{e} + \varepsilon_{33}^{e} = \tfrac{9}{2} b_1 I_1^{1/2} + 3 b_2 J_2. \tag{5}$$

Furthermore, the elastic volumetric strain can be further separated into two components, $\varepsilon_{v,p}^{e}$ and $\varepsilon_{v,s}^{e}$ as the following expression:

$$\varepsilon_{v,p}^{e} = \tfrac{9}{2} b_1 I_1^{1/2}, \tag{6}$$

$$\varepsilon_{v,s}^{e} = 3 b_2 \left(\sqrt{J_2}\right)^2, \tag{7}$$

where I_1 is a measure of hydrostatic stress and $\sqrt{J_2}$ is a measure of shear stress.

The shear strain $\left(\gamma = 2\sqrt{J_2'}\right)$ can also be determined based on Eq. (5) as

$$\gamma^{e} = 2\sqrt{J_2^{e'}} = 2(b_2 I_1 + b_3)\sqrt{J_2}. \tag{8}$$

Namely, the proposed Ω enables (1) non-linear volumetric deformation induced by hydrostatic stress (Fig. 4a); (2) non-linear volume dilation by shear stress (Fig. 4b); and (3) linear shear dilation (Fig. 4c). Accordingly, the material constants b_1, b_2 and b_3 can be determined by a curve fitting derived from the experimental curves, by PS test under a constant hydrostatic stress, as shown in Fig. 4. For the tested Tertiary sandstones, two *Type A* sandstones (WGS1 and MS2) and three *Type B* sandstones (WGS2, TL1 and CL) the corresponding b_1, b_2 and b_3 are summarized in Table 4. The ranges of b_1, b_2 and b_3 are $100–250 \times 10^{-6}\,(\mathrm{MPa})^{-1/2}$, $-0.7--0.1 \times 10^{-6}\,(\mathrm{MPa})^{-2}$ and $50–170 \times 10^{-6}\,(\mathrm{MPa})^{-1}$, respectively.

The factor b_1 alone controls the magnitude of elastic volumetric deformation induced by hydrostatic stress ($\varepsilon_{v,p}^{e}$), as revealed by Eq. (6). A greater b_1 increases the

Table 4
List of material parameters of the studied sandstones for the proposed constitutive model

Dry sandstone	WGS1	MS2	WGS2	TL1	CL
Elastic deformation					
b_1 (10^{-6}(MPa)$^{-1/2}$)	104.9	167.0	118.3	206.3	246.7
b_2 (10^{-6}(MPa)$^{-2}$)	−0.13	−0.17	−0.13	−0.26	−0.68
b_3 (10^{-6}(MPa)$^{-1}$)	56.7	65.5	75.5	103.0	165.5
Plastic deformation					
γ_D	0.11	0.12	0.14	0.12	0.10
T (MPa)	42.95	40.70	26.81	51.30	31.50
M	3.52	3.47	3.60	3.33	4.04
β_1	9.37E3	1.30E5	3.88E4	1.22E4	6.50E5
β_2	2.36	2.52	2.40	2.39	2.11
β_3	0.52	0.64	0.65	0.63	1.23
β_4	1.69E−07	7.34E−8	6.93E−08	4.02E−07	7.30E−11

amount of volumetric strain, as shown in Fig. 6a. Similarly, based on Eq. (7), the factor b_2 alone controls the amount of elastic shear dilation. A less b_2 increases the amount of shear dilation, as shown in Fig. 6b. The amount of elastic shear strain is jointly controlled by b_2 and b_3 by Eq. (8). A greater b_3 increases the amount of shear strain, as illustrated in Fig. 6c.

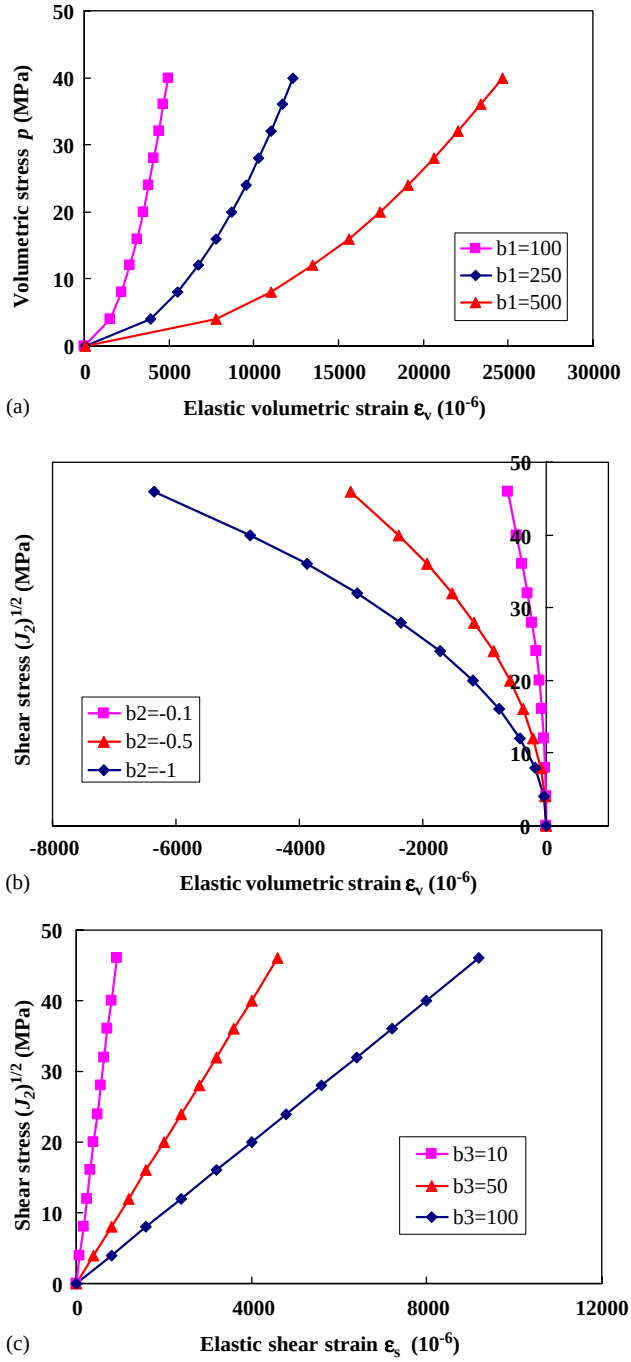

Fig. 6. Influences of the material parameters, b_1, b_2 and b_3 on the simulated elastic deformation based on the proposed model. The units of these parameters are shown in Table 4. (a) Elastic volumetric strain induced by hydrostatic stress, (b) Elastic volumetric strain induced by shear stress, (c) Elastic shear strain induced by shear stress.

4.2. Plastic component of deformation

If a plastic potential surface (or yield cap) with associated flow rule is assumed for the studied sandstones, the plastic potential surface will have the geometry, as illustrated in Fig. 6b. Similar yield surfaces have been proposed [33–36,7,11]. This coincidence reveals the similarity in the deformational nature of geo-material, including sandstones and soils.

An existing plastic model developed by Desai [37–38,8], which possesses a plastic potential surface similar to the above-mentioned features of the tested sandstone, is adopted and further modified. Assuming that the material has uniform strength on the deviatoric plane, the plastic potential surface for Tertiary sandstone is accordingly proposed to have the following simplified form:

$$F(I_1, J_2) = J_2 - \left[-\alpha_d (I_1 + T)^m + \gamma_d (I_1 + T)^2\right] = 0, \quad (9)$$

where T is the I_1 stress at which shear strength vanishes and m and γ_d are material constants controlling the geometry of the surface. The square root of γ_d represents the slope of the failure envelope, as illustrated in Fig. 7. In Eq. (9), α_d is a state parameter; it increases when the material is subjected to continuous loading and leads to the propagation of the plastic potential surface. Greater α_d represents a greater plastic potential surface, as depicted in Fig. 7. That is, the plastic potential surface propagates as the state variable α_d accumulates.

Meanwhile, since the plastic potential surface is capable of propagating when loading is continuously applied, a hardening rule is necessary and proposed as

$$d\varepsilon^p = \beta_1 \alpha_d^{\beta_2} + \left(\frac{\alpha_d}{\beta_4}\right)^{1/\beta_3}, \quad (10)$$

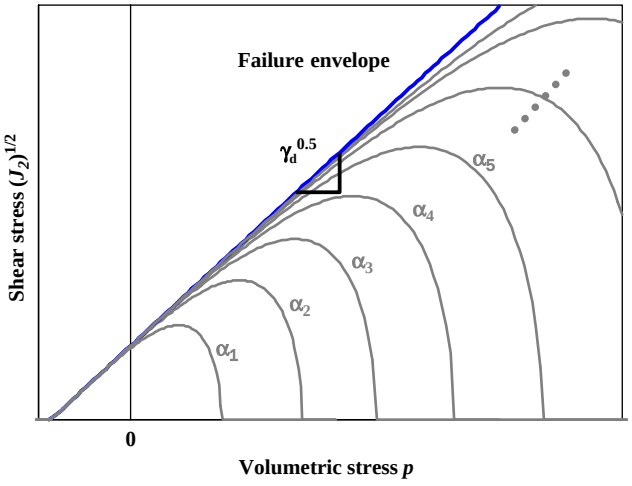

Fig. 7. Schematic illustration of the propagation of proposed plastic potential surfaces, in which α_1, α_2, α_3,... represent different magnitudes of the state variable α_d. $\sqrt{\gamma_d}$ represents the slope of the failure envelope.

where β_1, β_2, β_3 and β_4 are material constants controlling the magnitude of plastic strain increments.

Assuming that the associated plastic flow rule is applicable, the magnitude of plastic strain increment can then be expressed as

$$d\varepsilon^{p} = \lambda\left(\frac{\partial F}{\partial \sigma_{ij}}\frac{\partial F}{\partial \sigma_{ij}}\right)^{1/2} = \beta_1 \alpha_d^{\beta_2} + \left(\frac{\alpha_d}{\beta_3}\right)^{1/\beta_4}, \tag{11}$$

where λ is a positive scalar factor of proportionality.

Accordingly, the magnitude of plastic strain increment $d\varepsilon^{p}$, the plastic volumetric strain increment $d\varepsilon_v^{p}$ and the plastic shear strain increment $d\varepsilon_s^{p}$ can be obtained as

$$\mathrm{d}\varepsilon_v^{p} = 3\lambda\left(\frac{\partial F}{\partial I_1}\right) = \frac{3\mathrm{d}\varepsilon^{p}\left(\dfrac{\partial F}{\partial I_1}\right)}{\left(\dfrac{\partial F}{\partial \sigma_{ij}}\dfrac{\partial F}{\partial \sigma_{ij}}\right)^{1/2}} = \frac{3\left\{\beta_1\alpha_d^{\beta_2} + \left(\dfrac{\alpha_d}{\beta_4}\right)^{1/\beta_3}\right\}\left(\dfrac{\partial F}{\partial I_1}\right)}{\left(\dfrac{\partial F}{\partial \sigma_{ij}}\dfrac{\partial F}{\partial \sigma_{ij}}\right)^{1/2}}, \tag{12}$$

$$\mathrm{d}\varepsilon_s^{p} = \sqrt{(d\varepsilon^{p})^2 - \left(\mathrm{d}\varepsilon_v^{p}\right)^2}. \tag{13}$$

Based on Eqs. (9)–(13), the proposed plastic model has seven material parameters, with γ_d, T, m controlling the geometry of plastic potential surface and β_1, β_2, β_3 and β_4 controlling the magnitude of plastic strains. All these parameters can be obtained by a curve fitting derived from the experimental results. As for the detailed process of determining these material parameters, the reference can be found in Desai [8,37–38] and Jeng et al. [6]. These material parameters for the studied sandstones are also listed in Table 4. The ranges of γ_d, T, m, β_1, β_2, β_3 and β_4 are 0.10–0.14, 31–52 MPa, 3.3–4.1, 1.3×10^{-5}–9.37×10^{-3}, 2.11–2.40, 0.52–1.23, 7.3×10^{-11}–4.02×10^{-7}, respectively. The influence of β_2 and β_3 on the plastic volumetric strain and plastic shear strain is illustrated in Fig. 8. In general, greater β_3 results in greater shear contraction followed by dilation and a greater β_2 leads to greater volumetric strain.

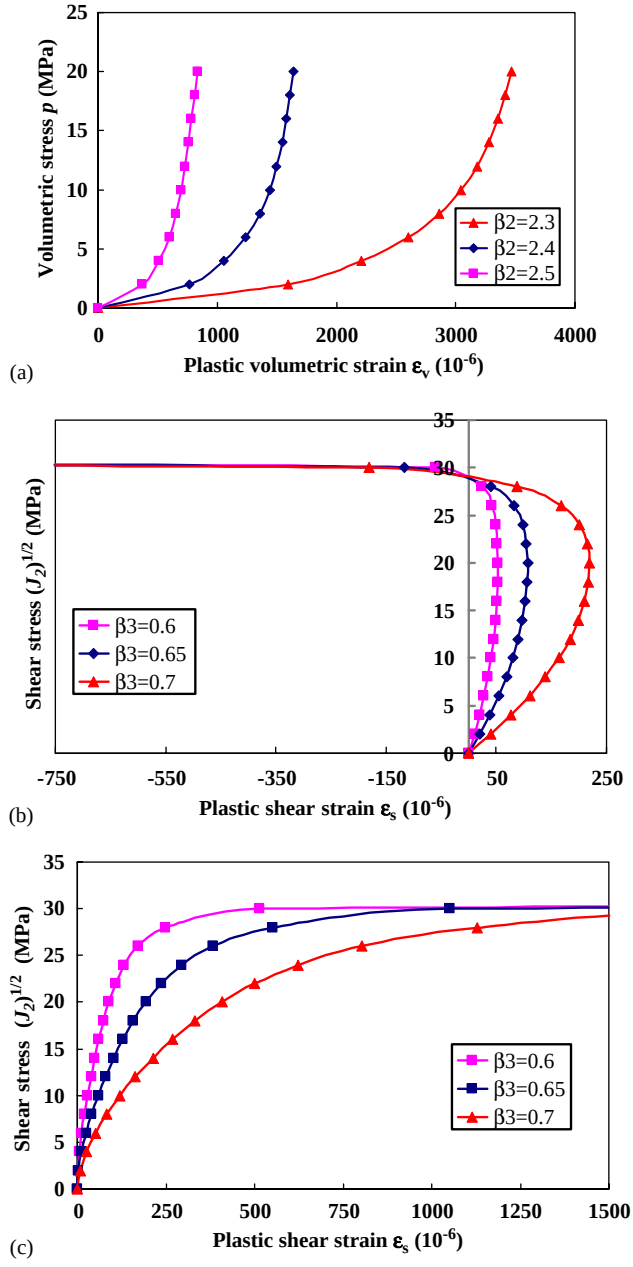

Fig. 8. Influences of the material parameters, β_2 and β_3 on the simulated plastic deformation based on the proposed model. (a) Plastic volumetric strain induced by hydrostatic stress, (b) Plastic volumetric strain induced by shear stress, (c) Plastic shear strain induced by shear stress.

4.3. Determination of parameters

The proposed model includes 3 elastic parameters (b_1, b_2 and b_3) and 7 plastic parameters (γ_d, T and m, determining the geometry of failure envelope and plastic yield surface; β_1, β_2, β_3 and β_4, determining the hardening rule).

For the elastic parameters, b_1 is determined from the elastic volumetric strain–volumetric stress relationship as shown in Fig. 4a. b_2 is determined from the elastic shear stress–shear strain relationship shown in Fig. 4c. Based on the determined b_1 and b_2, b_3 can then be obtained from Fig. 4b.

For the parameters determining plastic surfaces, γ_d can be obtained from the current stress state as

$$\gamma_d = \frac{J_2}{(I_1 + T)^2}. \tag{14}$$

Table 5
Summary of the analyzed constitutive models

	Proposed model	Drucker–Prager model	Extended Drucker–Prager model
Elastic deformation	$\varepsilon_{ij} = (\frac{\lambda}{2} b_1 I_1^{1/2} + b_2 J_2)\delta_{ij} + (b_2 I_1 + b_3) s_{ij}$	$\varepsilon_{ij} = \frac{1+\nu}{E}\sigma_{ij} - \frac{\nu}{E}\delta_{ij}$	$\varepsilon_{ij} = \frac{1+\nu}{E}\sigma_{ij} - \frac{\nu}{E}\delta_{ij}$
Plastic deformation			
Yield surface	$F_1(I_1, J_2) = J_2 - F = 0$ $F = [-\alpha_d (I_1 + T)^m + \gamma_d (I_1 + T)^2]$	$F_1(I_1, J_2) = \sqrt{J_2} - \alpha_f I_1 - k_f = 0$	$F_1(I_1, J_2) = \sqrt{J_2} - \alpha_f I_1 - k_f = 0$ $F_2 = R_c^2 J_2 + (I_1 - C)^2 = R_c^2 b^2$
Plastic potential surface	$G(I_1, \sqrt{J_2}) \equiv F(I_1, \sqrt{J_2})$	$G(I_1, \sqrt{J_2}) \equiv F(I_1, \sqrt{J_2})$	$G(I_1, \sqrt{J_2}) \equiv F(I_1, \sqrt{J_2})$
Hardening rule	$d\varepsilon^p = \beta_1 \alpha_d^{\beta_2} + \left(\frac{\alpha_d}{\beta_4}\right)^{1/\beta_3}$	Not available	$d\varepsilon^p = a_1 \exp(\eta_1 X)$

In turn, m can be determined from γ_d and the current stress state as

$$m = \frac{2\gamma_d}{\gamma_d - [J_2/(I_1 + T)^2]}. \quad (15)$$

For the hardening parameters, β_1 and β_2 can be determined from the increments of plastic strain during hydrostatic loading as

$$\ln(d\varepsilon^p) = \beta_1 + \beta_2 \ln(\alpha_d). \quad (16)$$

Finally, β_3 and β_4 can be determined from the following relationship during pure shearing:

$$\ln(d\varepsilon^p) = 1/\beta_3 [\ln(\beta_4) - \ln(\alpha_d)]. \quad (17)$$

5. Performance of the proposed constitutive model

To evaluate the performance of the proposed constitutive model, comparisons between simulated deformation and the actual deformation were conducted. In addition, the simulations of other existing models were also carried out and compared. In this way the characteristics of the proposed model could be highlighted. Accordingly, the D–P model and Cap model were included. The expressions determining the geometry of the failure envelope, plastic potential surface and hardening rules of the proposed model, DP model and D–P model with a cap (Extended Drucker–Prager model, EDP) are summarized in Table 5 for comparison.

Typical deformation curves obtained from experiments are shown in Figs. 9a, 10a and 11a, in which the deduced elastic and plastic components were also plotted. The simulated volumetric deformation induced by volumetric strain is shown in Fig. 9. Since conventional linear elasticity was incorporated into the other two models, they yielded a linear elastic volumetric deformation curve; however, the proposed model allowed the non-linear behavior and resulted in a reasonable volumetric deformation when compared to the actual one.

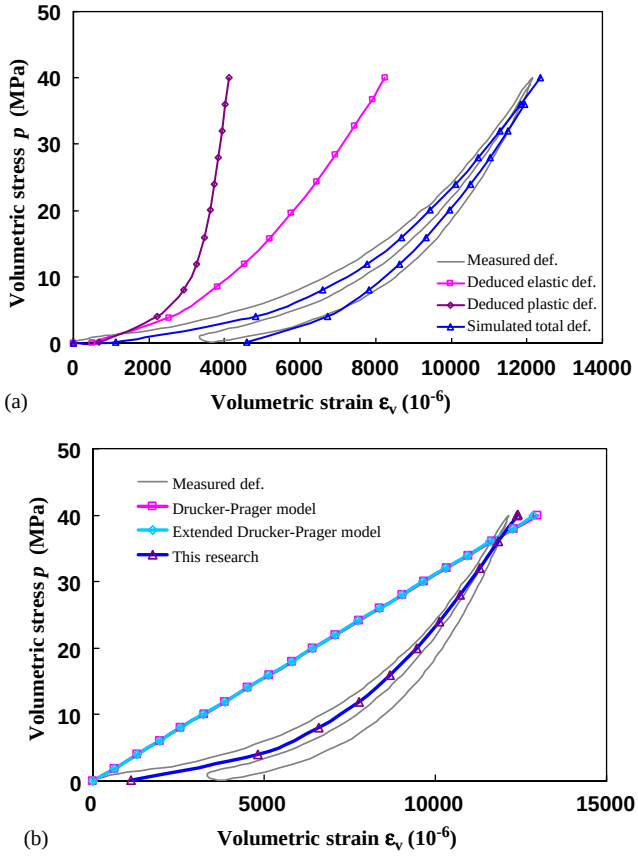

Fig. 9. Simulation of volumetric strain induced by hydrostatic stress using different models. (a) The total strain and the decomposed elastic and plastic components. (b) Simulation comparison for the proposed model and other two models. The sandstone is MS2.

As shear deformation was concerned, the simulations of the other two models had linear deformation prior to the failure state and were followed by significant plastic deformation, as shown in Fig. 10b. The proposed model enabled plastic deformation before the failure state and thus resulted in gradual transition before and after the failure state (Fig. 10b). As to the volumetric deformation induced by shearing, the proposed model was capable of simulating shear contraction and shear dilation, which is compared well to the actual deformation as illustrated in Fig. 11b (Table 6).

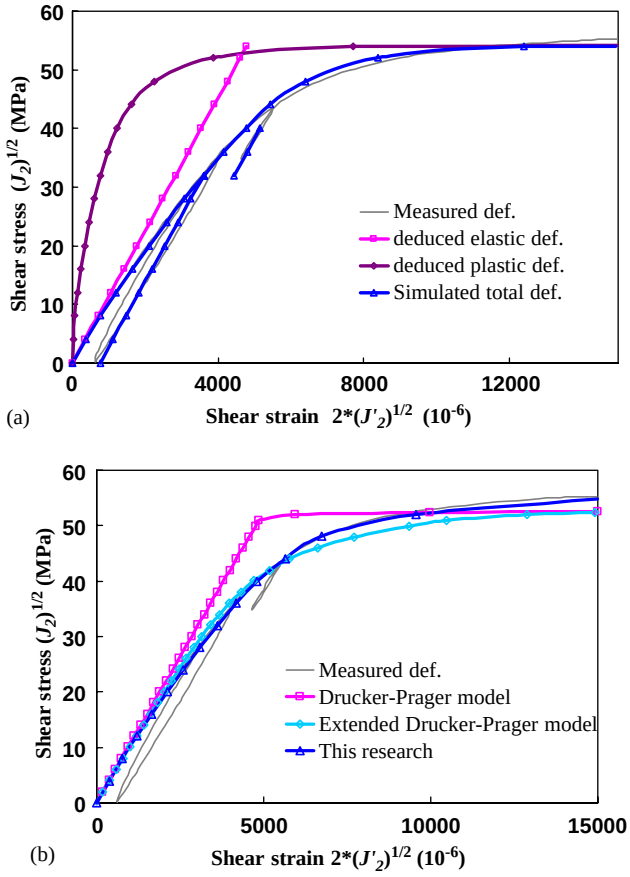

Fig. 10. Simulation of shear strain induced by shear stress using different models. (a) The total strain and the decomposed elastic and plastic components. (b) Simulations comparison for the proposed model and other two models. The sandstone is MS2.

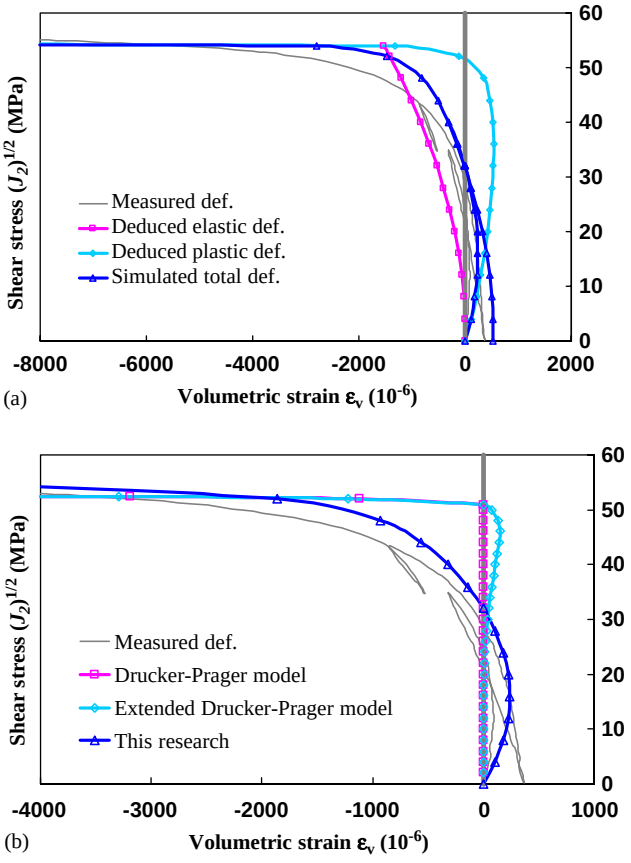

Fig. 11. Simulation of volumetric strain induced by shear stress using different models. (a) The total strain and the decomposed elastic and plastic components. (b) Comparison of the simulations obtained from the proposed model and other two models. The sandstone is MS2.

6. Discussion—influence of hydrostatic stress and stress path

Based on the result of comparison shown in previous section, the simulation of the proposed model is made under constant hydrostatic stress and sheared under pure shearing state (PS). It appears to meet the actual deformation reasonably well. It would be interesting to further investigate the performance of the proposed model under various hydrostatic stresses and stress paths, with material parameters obtained during one single test.

Fig. 12 shows the results of deformation simulation under various hydrostatic stresses, $p = 20$, 40 and 60 MPa, in which the material parameters were obtained from $p = 40$ MPa condition. It can be seen that the proposed model can also yield reasonable simulation close to the actual behavior, both in shear deformation (Fig. 12a) and in volumetric deformation (Fig. 12b) induced by shearing of other hydrostatic stress condition.

When triaxial tests, other than PS-typed, are concerned, the simulated and the actual types of deformation of CTC test, in which axial compression occurs, are shown in Fig. 13. The simulated results are still reasonably close to the actual deformation of CTC tests with some discrepancy exist. This discrepancy possibly arises from the slightly evolution of the actual yield surface or the heterogeneity of sandstone samples; however, since the discrepancy is minor, the assumption of a no-evolving yield surface seems to be acceptable. As the axial-elongation type of triaxial test is concerned, e.g., the RTE, Fig. 14 shows the comparison of the simulated and the actual deformation and again reveals that both of them are in a reasonably good agreement.

In summary, the tests over varying hydrostatic stress and stress paths indicate that the proposed model is capable of providing reasonable simulation under the above-mentioned situations.

7. Conclusion

Tertiary sandstones are characterized with significant elastic and plastic shear dilation. In addition to

Table 6
Material parameters of MS2 sandstone based on different material models

	Parameter	Magnitude
Elastic deformation		
Linear elasticity	K	3.1 GPa
	G	11.2 GPa
Non-linear elasticity (proposed model)	b_1	167.0×10^{-6} (MPa)$^{-1/2}$
	b_2	-0.17×10^{-6} (MPa)$^{-2}$
	b_3	65.5×10^{-6} (MPa)$^{-1}$
Plastic deformation		
Drucker–Prager model	α_f	0.34
	k_f	11.02 MPa
Extended Drucker–Prager model	R_c	1.67
	a_1	0.29
	η_1	0.05
Proposed model	γ_d	0.12
	T	40.70 MPa
	m	3.47
	β_1	1.30E−5
	β_2	2.52
	β_3	0.64
	β_4	7.34E−8

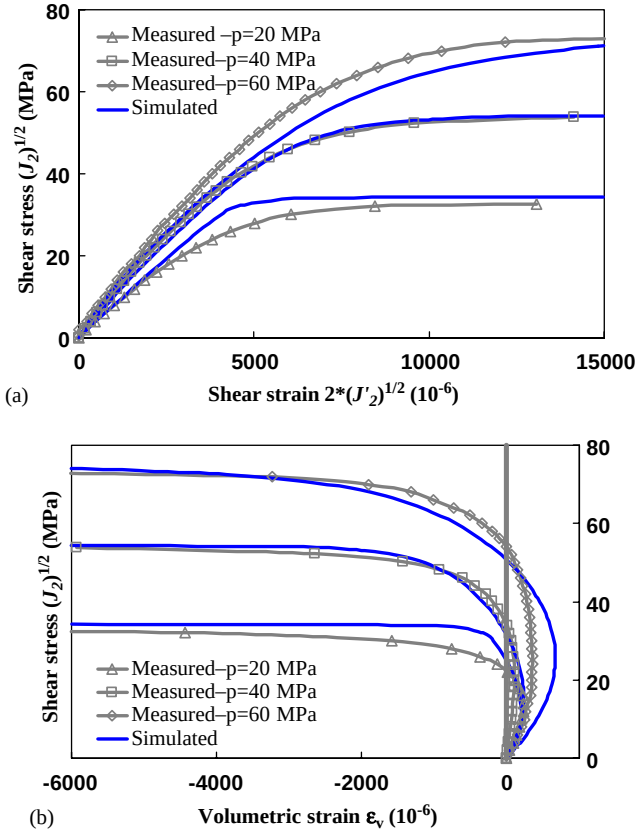

Fig. 12. Simulation of shear and volumetric strains induced by shear stress under different constant hydrostatic stress (PS tests). Figs. 12–14, the material parameters were obtained from PS test under $p =$ 40 MPa. The sandstone is MS2.

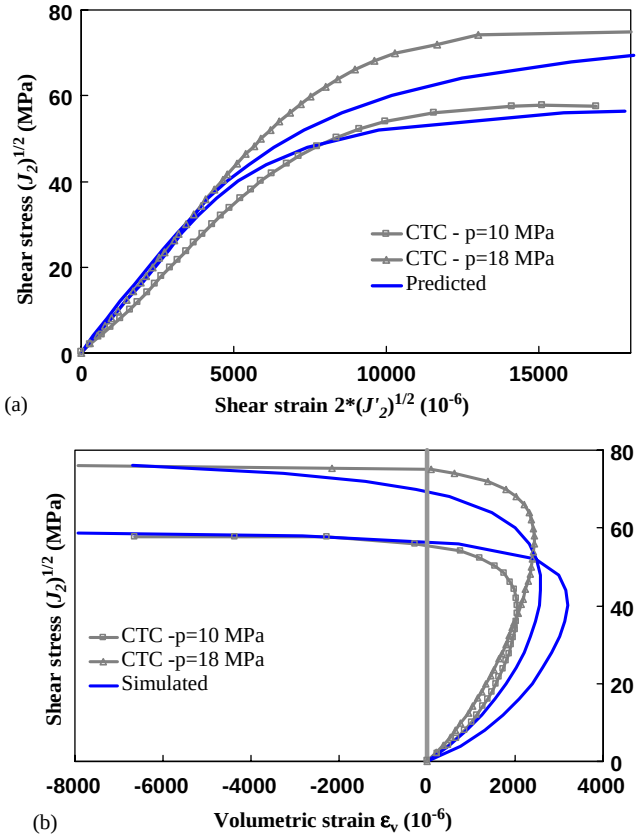

Fig. 13. Simulation of shear and volumetric strains induced by shear stress for CTC tests.

the dilation induced by hydrostatic stress unloading during tunnel excavation, this dilation contributes to the tunnel deformation, especially the crown settlement. This phenomenon indicates that, while allocating the source of tunnel squeezing for any type of rocks and as long as elastic shear dilation is significant, the vast unloaded elastic zone should be considered in addition to the plastic zone adjacent to the tunnel wall.

To simulate more sophisticated deformational behavior, the number of parameters increases simultaneously. In the proposed model, a total of 10 parameters are needed. However, tests on the model showed that one set of parameters obtained from one particular testing condition could be applied to various conditions, stress paths and hydrostatic stresses. This more or less reduces the efforts needed to determine the parameters. Furthermore, the applicability of the proposed model is not limited to Tertiary sandstones only. For any rock, as long as it possesses linear or non-linear plastic and elastic deformation, including shear dilation, and plastic potential surface similar to the ones shown in Fig. 5b, this model can be applied.

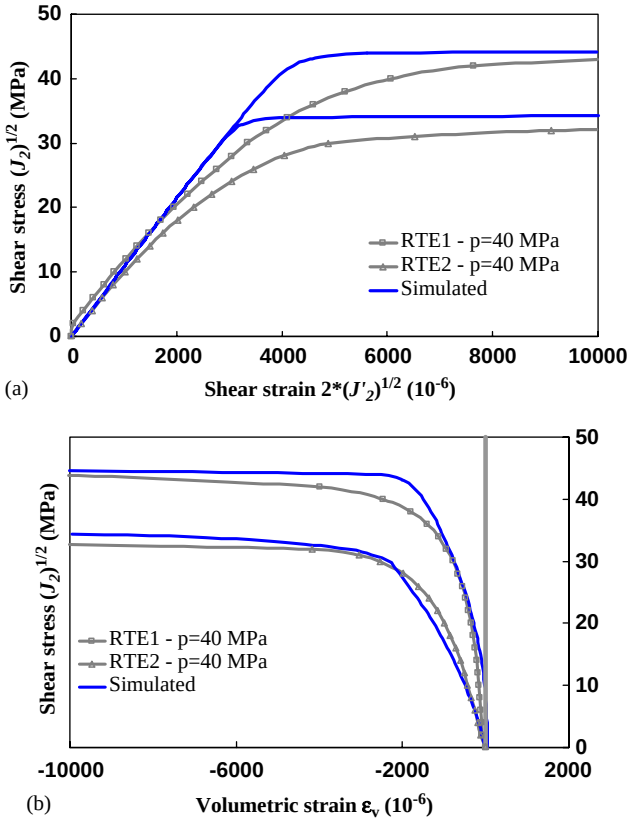

Fig. 14. Simulation of shear and volumetric strains induced by shear stress for RTE tests.

Acknowledgements

The research is supported by the National Science Council of Taiwan, Grant no. NSC-89-2211-E-002-152, NSC-90-2211-E-002-094 and NSC-91-2211-E-002-046. The considerable effort and valuable suggestions provided by the anonymous reviewers are gratefully acknowledged.

References

[1] Jeng FS, Ju GT, Huang TH. Properties of some weak rock in Taiwan. In: Proceedings of Taiwan rock engineering symposium, Taipei, 1994. p. 259–67 [in Chinese].
[2] Jeng FS, Lee IT, Huang TH. Deterioration of weak rock induced by wetting process. Proceedings of Taiwan rock engineering symposium, Taipei, 1996. p. 373–82 [in Chinese].
[3] Jeng FS, Huang TH. Time dependent behavior of weak sandstone on Mushan formation. In: Proceedings of the 13th Southeast Asian geotechnical conference, Taipei, 1998. p. 75–80.
[4] Jeng FS, Huang TH. Shear dilatational behavior of weak sandstone. In: Proceedings of regional symposium on sedimentary rock engineering, Taipei, 1998. p. 262–7.
[5] Jeng FS, Weng MC, Huang TH, Lin ML. Deformational characteristics of weak sandstone and impact to tunnel deformation. Tunnelling Underground Space Technol 2002;17:263–74.
[6] Jeng FS, Weng MC, Lin ML, Huang TH. Influence of petrographic parameters on geotechnical properties of Tertiary sandstones from Taiwan. Eng Geol 2004;73:71–91.
[7] Lagioia R, Nova R. An experimental and theoretical study of the behaviour of a calcarenite in triaxial compression. Géotechnique 1995;45:633–48.
[8] Desai CS, Salami MR. A constitutive model and associated testing for weak rock. Int J Rock Mech Min Sci Geomech Abstr 1987;24:299–307.
[9] Papamichos E, Tronvoll J, Vardoulakis I, Labuz JF, Skjærstein A, Unander TE, Sulem J. Constitutive testing of red Wildmoor sandstone. Mech Cohes-Frict Mater 2000;5:1–40.
[10] Hawkins AB, McConnell BJ. Sensitivity of sandstone strength and deformability to changes in moisture content. Q J Eng Geol 1992;25:115–30.
[11] Lagioia R, Puzrin AM, Potts DM. A new versatile expression for yield and plastic potential surfaces. Comput Geotech 1996; 19(3):171–91.
[12] Sulem J, Vardoulakis I, Papamichos E, Oulahna A, Tronvoll J. Elasto-plastic modeling of red Wildmoor sandstone. Mech Cohes-Frict Mater 1999;4:215–45.
[13] Vatsala A, Nova R, Srinivasa Murthy BR. Elastoplastic model for cemented soils. J Geotech Geoenviron Eng 2001;127(8): 679–87.
[14] Lade P. Elasto-plastic stress–strain theory for cohesionless soil with curved yield surfaces. Int J Struct 1977;13:1019–35.
[15] Kim MK, Lade PV. Modelling rock strength in three dimensions. Int J Rock Mech Min Sci Geomech Abstr 1984;21:21–33.
[16] Gerogiannopolous N, Brown ET. The critical state concept applied to rock. Int J Rock Mech Min Sci Geomech Abstr 1978;15:1–10.
[17] Brown ET, Michelis PN. A critical state yield equation for strain softening rock. In: Proceedings of the 19th US symposium on rock mechanics, Lake Tahoe, Nevada, 1978. p. 515–9.
[18] Price AM, Farmer IW. Application of yield models to rock. Int J Rock Mech Min Sci Geomech Abstr 1979;16:157–9.
[19] Dragon A, Mroz Z. A continuum model for plastic-brittle behavior of rock and concrete. Int J Rock Mech Min Sci Geomech Abstr 1979;16:253–9.
[20] Ichikawa Y, Yamabe T, Obara Y, Ito F, Kawamoto T. Brittle-ductile fracture of a tuffaceous rock and plasticity theory. In: Desai CS, Gallagher RH, editors. Proceedings of the international conference on constitutive laws for engineering materials. Tucson: Arizona; 1982. p. 349–55.
[21] Brace WF, Paulding BW, Scholz C. Dilatancy in the fracture of crystalline rocks. J Geophys Res 1966;71:3939–53.
[22] Hardy Jr HR, Kim RY, Stefanko R, Wand YJ. Creep and microseismic activity in geologic materials. In: Proceedings of the 11th symposium on rock mechanics (AIME) 1970. p. 377–414.
[23] Goodman RE. Introduction to rock mechanics. New York: Wiley; 1989.
[24] Martin CD, Chandler NA. The progressive fracture of Lac du Bonnet Granite. Int J Rock Mech Min Sci 1994;31:643–59.
[25] ISRM Ltd. In: Brown ET, editor. Rock characterization testing & monitoring—ISRM suggested methods. New York: Pergamon; 1981.
[26] Aristorenas GV. Time-dependent behavior of tunnels excavated in shale. Doctoral thesis, Department of Civil Engineering, Massachusetts Institute of Technology, MA, USA, 1992.
[27] Bernabe Y, Fryer DT, Shively RM. Experimental observations of the elastic and inelastic behaviour of porous sandstones. Geophys J Int 1994;117:403–18.
[28] Bésulle P, Desrues J, Raynaud S. Experimental characterization of the localisation phenomenon inside a Vosges sandstone in a triaxial cell. Int J Rock Mech Min Sci Geomech Abstr 2000; 37:1223–37.

[29] Dyke CG, Dobereiner L. Evaluating the strength and deformability of sandstones. Q J Eng Geol 1991;24:123–34.
[30] Handin J, Hager RV. Experimental deformation of sedimentary rock under a confining pressure tests at room temperature on dry samples. Bull Am Assoc Pet Geol 1957;41:1–50.
[31] Chen WF, Saleeb AF. Constitutive equations for engineering materials, vol. I: elasticity and modeling. New York: Wiley; 1982.
[32] Pettijohn FJ, Potter PE, Siever R. Sand and sandstone. Berlin: Springer; 1987 306pp.
[33] DiMaggio ML, Sandler IS. Material model for granular soils. J Eng Mech Div ASCE 1971;97:935–50.
[34] Mullenger G, Davis RO. An unified yield criterion for cohesionless granular materials. Int J Numer Analytical Methods Geomech 1981;5:285–94.
[35] Gens A, Nova R. Conceptual bases for a constitutive model for bonded soils and weak rocks. In: Anagnostopoulos, et al., editors. Geotechnical engineering of hard soils-weak rocks. Rotterdam: Balkema; 1993. p. 485–94.
[36] Zhang J, Wong TF, Davis DM. Micromechanics of pressure-induced grain crushing in porous rocks. J Geophys Res 1990; 95(B1):341–52.
[37] Desai CS, Varadarajan A. A constitutive model for quasi-static behavior of rock salt. J Geophys Res 1987;92:11445–56.
[38] Desai CS, Somasundram S, Frantziskonis G. A hierarchical approach for constitutive modeling of geologic materials. Int J Num Anal Methods Geomech 1986;10:225–57.